Photoproduction Cross-section of the $\eta^{'}$ meson with CLAS

M.Sc. Thesis

By

Saeed Ahmad

DISCIPLINE OF PHYSICS

INDIAN INSTITUTE OF TECHNOLOGY INDORE

JULY 2016

Photoproduction Cross-section of the $\eta^{'}$ meson with CLAS

A THESIS

Submitted in partial fulfillment of the requirements for the award of the degree

of

Master of Science

by

Saeed Ahmed

DISCIPLINE OF PHYSICS

INDIAN INSTITUTE OF TECHNOLOGY INDORE

JULY 2016

INDIAN INSTITUTE OF TECHNOLOGY INDORE

CANDIDATE'S DECLARATION

I hereby certify that the work which is being presented in the thesis entitled " **Photoproduction Cross-section of the η' meson with CLAS**" in the partial fulfillment of the requirements for the award of the degree of **MASTER OF SCIENCE** and submitted in the **DISCIPLINE OF PHYSICS, Indian Institute of Technology Indore**, is an authentic record of my own work carried out during the time period from July, 2015 to July, 2016 under the supervision of Dr. Ankhi Roy, Associate Professor, Discipline of Physics, IIT-Indore.

The matter presented in this thesis has not been submitted by me for the award of any other degree of this or any other institute.

(Saeed Ahmad)

This is to certify that the above statement made by the candidate is correct to the best of my/our knowledge.

(Dr. Ankhi Roy)

Mr. Saeed Ahmad has successfully given his M.sc. Oral Examination held on ....

(Thesis Supervisor) (Convener, DPGC)

Date: Date:

(PSPC Member) (PSPC Member)

Date: Date:

Acknowledgement

First and foremost, I would like to thank almighty God by saying that may all of his blessing be upon us. I would like to deeply thank my supervisor Dr. Ankhi Roy for all great advice and support throughout my time here at IIT Indore. I would like to thank my parents to improve my perception. I also would like to thank all the Faculties of Indian Institute of Technology Indore Physics department specially Dr. Subhendu Rakshit, Dr. Manavendra Mahato, Dr. Raghunath Sahoo, for creating a great atmosphere for learning and growth in my knowledge.

I would like to thank Mr. Sudeep Ghosh for helping me through many suggestion in handling with data. Many thanks to Ms. Ankita Goswami and Ms. Sujata Pandey for their great conversation, Mr. Ajay Kumar, Mr. Samsul Islam, and Mr. Sudhir Rode for good time during my research. Moreover, I also would like to thank all Particle Physics researchers including experimental and theoretical and all my classmates, who were wonderfully helpful to me during my work. At the end of the day I would like to thank Google for it's accessibility and help me at every points.

Dedicated

to

My Family

Abstract

Quantum Chromodynamics (QCD) is the theory of strong interaction, which is a fundamental force to hold nucleons inside the nucleus. The coupling strength is very large at low momentum transfer regime of QCD compare to high momentum and hadrons are the degrees of freedom in this regime. So, the study of hadronic decay of different light mesons(π^0, η, $eta^{'}$) is very useful tool to explore the low energy regime of QCD. Photoproduction of the $\eta^{'}$ meson has been studied in the present work using Continuous Electron Beam Accelerator Facility(CEBAF) and the CLAS detector setup at Jefferson Lab, USA. Tagged photon beam of energy from 1.2 GeV to 5.5 GeV and hydrogen target of length 40cm and radius 2cm have been used for the photoproduction of light mesons $(\pi, \omega, \eta, \eta^{'}, \phi)$ in this experiment. Main physics motivation of this project is to determine differential cross-section of the $\eta^{'}$ meson using the channel $\eta^{'} \longrightarrow \eta\pi^+\pi^-$ from beam energy 1.2 GeV to 5.5 GeV. All the final state charged particles(p, π^+, π^-) and neutral particles are detected by the CLAS spectrometer. Finally two charge particles and any number of neutral particles along with proton (p) have been used as a selection criteria for data skimming from huge data set. A missing mass technique from the kinematical information of proton, and two pions π^+, π^- has been used to reconstruct the η meson of final state. Missing mass of the η meson from mean ($\mu = 548\ GeV/c^2$) to $\pm 3\sigma$ ($\sigma = 10 MeV/c^2$) and invariant mass of $\pi^+\pi^-$ 0.3 GeV to 0.6 GeV have been selected to reduce background from other channels. Total number of the $\eta^{'}$ meson has been estimated after the efficiency correction. Then differential cross-section has been calculated and compared with previous published measurement.

Contents

List of Figures

Chapter 1

Introduction

To know and understand, what is inside the matter at its most fundamental level(atom), it is necessary to probe or scatter the atom. As Rutherford performed the experiment by scattering beam of energetic particles with Gold foil, and able to measure recoilling byproduct using detector. On the basis of outcome he was able to demonstrate that there is a tiny positive region centered to the atom consists of whole mass of atom.
After his proposal people thought that, if nucleus is consist of more than one positive charge(proton); why they can't escape from nucleus because of repulsion? Why combination of nucleons form a bound state? Is there any other force acting between them, which is more stronger than electrostatic force? Yukawa formulated an elegant theory [**?**] known as Yukawa's meson theory, which tells that there is a strong force acting between nucleons mediated by meson(middle mass particle). The muonμ was discovered in 1936 [**?**], shortly after Yukawa's theory was published. It carries the same electrical charge as electron, but mass about hundred times the mass of electron. After these discoveries, there were another long "strange meson" so called kaon K found. With these discoveries, the landscape consisted nearly a dosen of 'elementary particles', all of which were required experimental results. Thus suspicions were mounting that these states were the expression of a more fundamental physics. After this exposure there had been so many particles discovered as the time went on.

1.1 The Quark Model

After discovering so many particles, people tried to fit them in a pattern like periodic table of atom. Astonishingly particles were followed the pattern eg. Eightfold way as shown in Figure ??. The Eightfold way arranged the baryons and mesons into weird geometrical pattern according to their charge and strangeness.Here in Figure ?? eight lightiest baryons fit into a hexagonal array. This group is known as baryon octet. Similarly eight litest mesons fill in hexagonal pattern, forming meson octet.

But the very success of Eightfold way begs the question: why do the hadrons fit into these bizare pattern? So; to resolve this problem Gell-Mann and Zweing independently proposed that all hadrons are infact composed of more elementary particles called quark [?]. The next job was to arrange quarks arithmetically. In doing this people got some particles which were not member of supermultiplet eg. $\eta^{'}$, and it is singlet state [?].

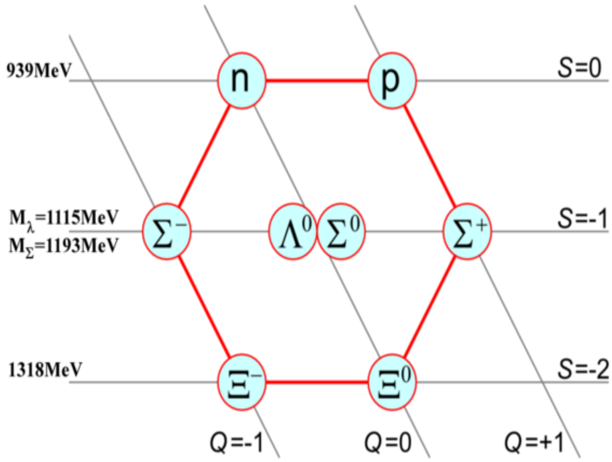

Figure 1.1: The baryon octet having eight lightiest baryon. They arranged in a pattern. The charge is -1 to +1 from left to right, and strangeness is 0 to -2 from top to bottom.

The entire gesture of particle physics is not over. What are the theory associated with different interactions? The theory that belongs to Electromagnetic force is Electrodynamics, and for Strong force the theory is Chromodynamics. At their quantum level these theories are so called Quantum Electrodynamics(QED), and Quantum Chromodynamics(QCD). The QED is well devoloped theory, and is spectacularly successful in explaining the experimental results, where as QCD is still in puzzle and undetermined.

As for as my job is concern, it is basically fall in the era of high energy. The high energy is actually the amount of energy by which we can probe inside the nucleus, I mean we can go where the strong interaction is envolved. So the theory associated with my experiment is QCD.

1.2 Quantum Chromodynamics(QCD)

Unlike the interaction in QED where mediator is photon and coupling strength is constant $\alpha = 1/137$; In QCD the mediators are gluons and coupling strength α_s is varying according to the momentum transfer. It varies around 1, eg. as α_s determined from force between two protons, it is greator than 1, and the bigness of this number has plagued particle physics for a decade. Due to this variation, there are two important feature associated with QCD.

(1) Quark Confinement

(2) Asymtotic Freedom

In the Figure ??, the variation between α_s and Q(the momentum transfer between nucleons or quarks) looks like, the value of α_s is very large when momentum transfer Q is very less. On the other hand if Q is very large, α_s is very less, and it is asymtotically constant. For larger value of α_s quarks are confined into hadronic state, where as for small α_s quarks are free from bound state of hadron. So at high energy the Perturbative QCD is theory working, as the coupling strength α_s is small. Where as for small energy the coupling strength α_s is large, the theory of Nonperturbative QCD comes into picture. As for as our experiment is concern, it is actually the energy domain which is well above the region controlled by low energy theorem [?]. On the other hand, it is for below the region of perturbative QCD [?, ?, ?, ?]. This energy range is important, because in this domain the various baryon resonance and coupled channel effect may play an important role in strangeness photoproduction. It is also important to conduct strangeness production experiment, to establish the quantum number of known states, as well as to search missing baryon resonance.

In our experiment, we analysed the channel $\eta' \longrightarrow \eta\pi^+\pi^-$, which is more relevant than channel $\eta' \longrightarrow \eta\pi^0\pi^0$, because in former case more phase space is available. We will discuss this in Chapter[3]. On the otherhand we can illustrate OZI rule. Which states that the production mode is supressed due to disconnected quark graph [?].

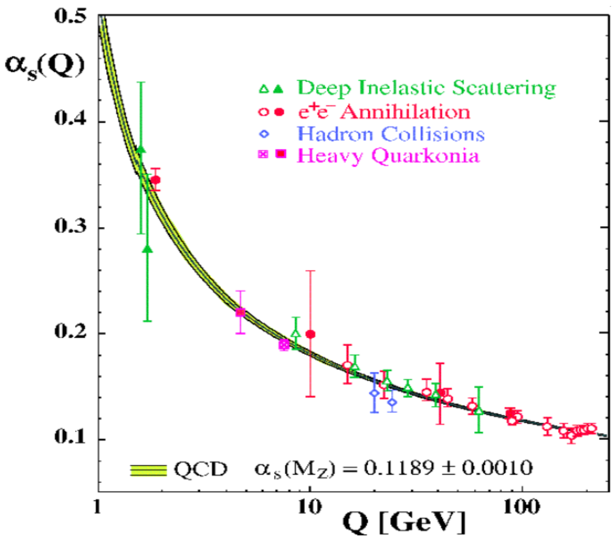

Figure 1.2: The variation of coupling strength α_s with momentum transfer Q in strong interaction.

Moreover, charges are positive and negative in QED where as in QCD there is another quantum number called color charge including positive and negative charge. The strong force is mediated by gluons. These gluons carry color and anticolor combination, because of this they are eight types, and they can interact with eachother Figure **??**.

1.3 Eta (η) and Etaprime (η') meson

Eta (η) and Etaprime (η') mesons are members of fundamental meson nonet. There are few properties associated with them shown in Table **??**

Eta η and Etaprime η' are pseudosalar mesons. They consist scalar property because they are spin zero particles. On the otherhand they transform like a vector under parity, because their corresponding parity eigen value is -1 [?]. As such they share many motivations of the exten-

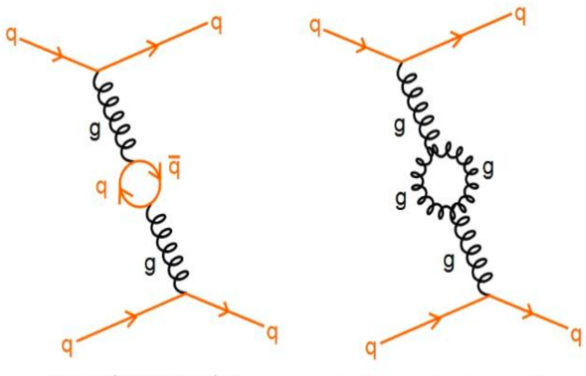

Figure 1.3: The interaction between quark-quark and gluon-gluon in strong interaction.

S.N.	Particle	Quark Content	Mass	Mean Life	Main Decay
1	η	$\frac{u\bar{u}+d\bar{d}-2s\bar{s}}{\sqrt{6}}$	547.862 $\pm 0.01 MeV/c^2$	(5 ± 0.3) $*10^{-19}s$	$\gamma\gamma$, $\pi^0\pi^0\pi^0$, $\pi^-\pi^+\pi^0$
2	$\eta^{'}$	$\frac{u\bar{u}+d\bar{d}+s\bar{s}}{\sqrt{3}}$	957.78 $\pm 0.02 MeV/c^2$	(3.2 ± 0.2) $*10^{-19}s$	$\pi^-\pi^+\eta$ $\pi^-\pi^+\gamma$ $\pi^0\pi^0\gamma$

Table 1.1: Properties of Eta(η) and Etaprime($\eta^{'}$) mesons

sive pion(π)photoproduction. These mesons differ from other mesons as they are consist of strange quarks. However, their strangeness number is zero/no net strangeness. This difference could help to determine the role of strange quark in the quark model properties of nucleons. Futhermore, isospin selectivity of η and $\eta^{'}$ mesons provide a tool to deconvolute the nucleon resonance spectrum in order to better isolate N^* nucleon resonance [?].

The data to be presented here is g-12 data, were obtained at the Thomas Jefferson National Accelerator Facility(J-Lab). In this analysis the beam energy is lying between respective threshold upto 5.4GeV. All the data taken by CLAS(CEBEF Large Acceptance Accelerator Facility). The unique capability of CLAS offered a great opportunity to provide differential cross-section of η and $\eta^{'}$.

1.4 Physics Motivation

The basic idea of deep exclusive meson photoproduction is that at $Q^2 >> 1GeV^2$ the meson is produced predominantly in configration of a tranverse size much smaller than its natural hadronic size i.e $r << R_{hadron} \sim (1fm)$.

The photoproduction thus probes the structure of nucleons locally and can be thought of as "local operator". This local operator thus induces transition between nucleon states. So by choosing the meson with approperiate quantum number, one can in this way probe nucleon structure with operator that are not accessible through the usual transverse spin structure , matter vs. charge distribution etc. Also, measurement of η and $\eta^{'}$ meson photoproduction on the proton target are supplying an "isospin filter" to nucleon resonance spectrum, due to isoscalar nature of these meson. This is because there are two types of interactions taking place in photoproduction experiment. Initially, when photon interacts with stationary proton the interaction known as electromagnetic interaction. The resonance state thus can be spin 1/2 or 3/2 as there ristriction on spin conservation in electromagnetic interaction. However, resonace state can only follow strong interaction beacause of their life time. Therefore, the spin zero final eg.(η and $\eta^{'}$) with proton only come from spin 1/2 resonace states. So, finding differential cross-section is an indirect tool to study the resonace spectrum.

Chapter 2

Experimental setup

The data used described in this project was accessed from CLAS experiment JLab. This data acquired during the experimental run period ‘g12‘ by CLAS detector. The whole setup is located in Newport News, Virginia. The aerial view of whole experimental setup is shown in Figure **??**. It consists of two main components.

(a) Continuous Electron Beam Accelerator Facility(CEBAF).

(b) CEBAF Large Acceptance Spectrometer(CLAS).

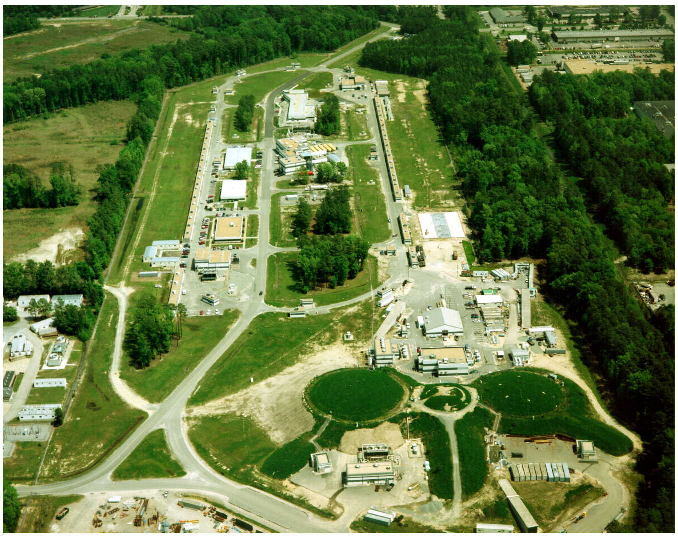

Figure 2.1: Aerial view of JLab

In this chapter we will discuss about parts of CLAS the experimental setup one by one.

2.1 Accelerator

CEBAF is an accelerator providing continuous wave of electron beam with energy up to 6 GeV. It also provides about 200μA of electric current to three experimental Hall A, B and C.

In CEBAF, a Superconducting Radio Frequency(SRF) cavities have been used to provide the acceleration gradient. Superconducting material is used here, because due to this, there is no resistive heating or unwanted things happen. It is made up of two niobium klystrons.

A positive potential is applied across each cavity so that as electron beam passes through it, provide constant acceleration gradient. The full diagram of CEBAF has been shown in the Figure **??**. CEBAF was the first

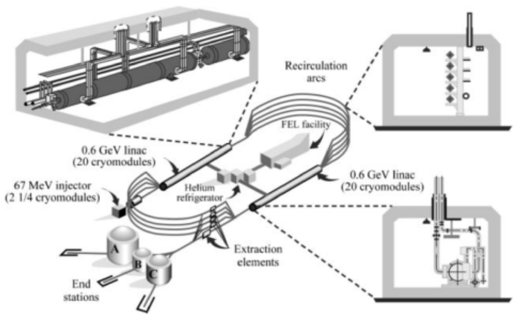

Figure 2.2: Continuous Electron Beam Accelerator Facility

accelerator that used in large scale application of superconducting radio frequency to investigate the quark structure of hadrons [**?**]. It consists of a polarized electron source, an injector and SRF. Two superconducting RF linear accelerators connected to each other by two arc sections containing steering magnet, with total track length of around 1400 m. CEBAF used liquid helium to cool SRF cavities to about 2K. This low temperature removes resistive consequences and allows system for most efficient transfer of energy to the electron.

The electron beam has been generated by illuminating GaAs photocathode with laser pulses. The laser pulses are temporally such that each experimental hall is able to receive electron bunches. The CEBAF operates at frequency about 1500 MHz. It is delivering beam to each experimental hall at frequency around 500 MHz, i.e. one third of CEBAF frequency. This allows each hall to operate simultaneously. This also delivers beam with 120 degree in phase [?]. Since the pulses are so short and close together that their propagation seems continuous.

The injector used in CEBAF is having elements related to bunching and timing of the beam so that work function match of element matches with beam. The beam started with 100 KeV from photo-cathode goes to the prebuncher cavity followed by emittance limiting apparatus. The chopper controls to the initial timing of beam and its longitudinal structure. The chopper operates at 500 MHz, so that any beam outside this window would not go forward through bunching process. The buncher starts bunching the beam coming after chopper. The capture section provides energy up to 500 KeV to the beam. In the next the beam further energies to 5 MeV by two SRF cavities. At the end there are two accelerating modules, each associates 8 SRF cavities. Therefore, the beam passes through it gained energy up to 68 MeV. The acceleration of beam through

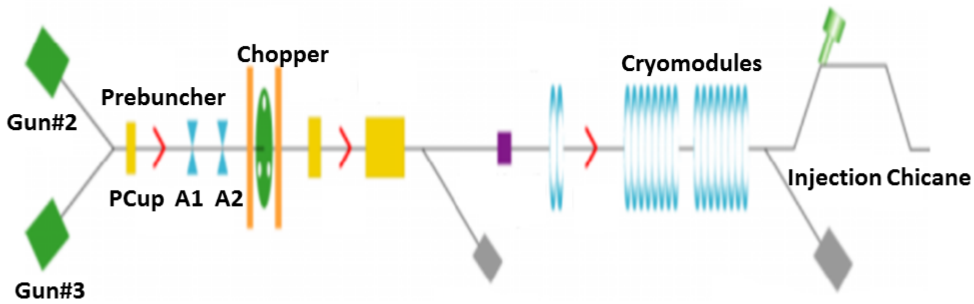

Figure 2.3: Injector with photo producing, bunching and accelerating components for electron beam

SRF is based on attraction phenomenon. A standing electromagnetic wave has been induced to accelerate the beam. The acceleration gradient caused by each sell of SRF reflect as energy in beam. Actually, the acceleration gradient is the ability to boost the energy of electron by a given amount within given length.

Moreover, the SRF cavity kept at very low temperature, so that it can take care of increase in temperature due to generated heat from acceleration

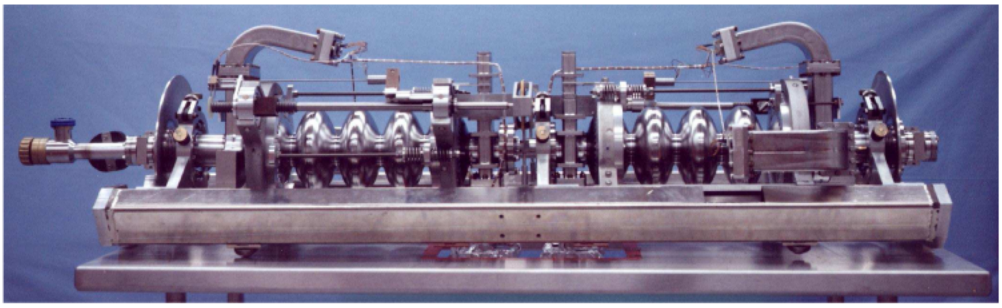

Figure 2.4: A picture of typical cavity used in CEBAF, made up of superconducting niobium klystron. An alternating potential is applied in this, provide standing electromagnetic wave within the cavity. The superconducting wall ensures that the energy of electromagnetic wave, only transfer to the beam passing through it.

gradient. After coming out from SRF cavity, the beam arrives at bending arc, which is located at both ends of linac. There are five bending arcs on one side and four on the other side, as shown in Figure **??**. It is magnetic re-circulating arcs bend and re-circulate the beam. These magnetic arc requires different magnetic field strength depending upon energy of incoming electron beam. In bunch of electrons, there are different sets with different energy. A chicane magnet(magnet used as temporary barrier, specially one design to reduce speed) at the end of each linac, separates the beam into their different mono-energetic path. After completing different path the beam merged back at same energy. This process is called recombination of beam which is done by the re-combiner magnet. The recombined beam then passes through another linac. The linac further accelerates the beam. This accelerated beam further passes through arc of second side. Again by the similar way the beam separated and recombined to acquire same energy. After completing one cycle the beam gained by 1.2 GeV. So that at the end of fifth cycle the beam acquires 6 GeV energy. This beam energy is considerable for our reaction purpose. After completing this much amount of energy, the beam allowed to go to different halls. There are three halls associated with experimental setup named as Hall-A, Hall-B and Hall-C for different purpose. Some of them is for electro-production and Hall-B is specially for photoproduction. Thus CEBAF can work both way, in electro-production as well as photoproduction. For our case the experimental purpose is to photon beam to interact with target. So after here we will only talk about photoproduction and Hall-B.

Hall-B houses two detectors, a photon tagger and CLAS. The tagger measures the event and beam energy in the photoproduction experiment. Where as CLAS i.e CEBAF Large Acceptance Spectrometer is the spectrometer use to detect final state particles.

Tagger:- It consists of dipole magnet combined with hodoscope. The dipole field allows to pass electrons with energy(E_e) between 20% to 95% of beam energy delivered by CEBAF.

The beam after passing through tagger incident on the radiator of gold foil. This type of radiation is called bremsstraghlung radiation. The bremsstraghlung radiation is the radiation occurs when electron bean accelerates by magnetic field of nuclei. In our experiment gold nuclei is used because it very ductile and it's atomic size is large. The less thickness reduces secondary emission and larger size reduces interaction among electron of beam and electron of atom. The energy of bremsstraghlung photon can calculated by using energy conservation. If E_{in} is the energy of incoming electron and E_{out} is the energy of outgoing electron, the energy associated with outgoing photonE_γ will be.

$$E_\gamma = E_{in} \text{ - } E_{out}$$

But after electron beam interacts with radiator, the outgoing one have mixture of photons as well as scattered electrons and un-scattered electrons. We now need to separate these electrons from beam and allow to collimate the bremsstraghlung photons. To remove the outgoing electrons from outgoing beam a dipole magnet is used; it does affect the photons. This bremsstraghlung photon then allowed to in interact with liquid hydrogen target.

2.2 Liquid Hydrogen Target

The target used in g12 experiment was cylindrical in shape as shown in Figure ??; it's length and diameter was 40cm and 4 cm respectively. It is positioned at the centre of CLAS spectrometer. This position enables the optimization of CLAS for small angle track detection. The target used as proton, because we can avoid interaction between electron of hydrogen and photon. The density of the target used in g12 is shown in Figure ??

Figure 2.5: The liquid hydrogen target used as proton target for experimental purpose.

After interaction from proton target, there are different types of particles

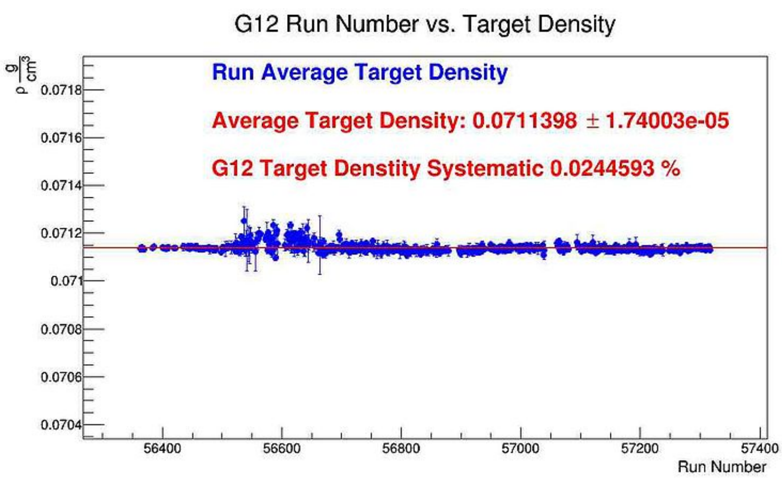

Figure 2.6: The liquid hydrogen target density used in g12 experiment.

produced, depending upon their threshold energy. The beam photon energy is shown in Figure ??. It is varying inversely proportional to beam photon energy.

$$\frac{\mathrm{d}N_\gamma}{\mathrm{d}E_\gamma} \propto \frac{1}{E_\gamma} \tag{2.1}$$

Where:

N_γ: Number of outgoing photon

E_γ: Lab energy of bremsstrahlung photon

Similarly:

$$\frac{\mathrm{d}N_\gamma}{\mathrm{d}W} \propto \frac{W}{W^2 - m_p^2} \tag{2.2}$$

Where:

W: Energy in CM frame; W = $\sqrt{m_p^2 + 2m_pE_\gamma}$.

After production of different types of particles(e.g. charged, neutral), we

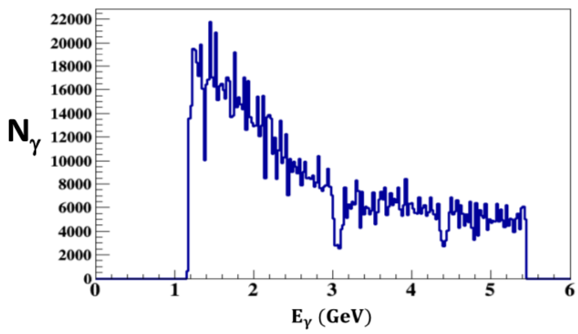

Figure 2.7: Variation of N_γ vs. E_γ

have to detect these particles. To detect particles,there are different elements have been used in CLAS detector setup.

2.3 CLAS Detector

"CEBAF Large Acceptance Spectrometer" abbreviated by "CLAS" is used to detect produced particles. As for as it's name is concern, it covers almost 4π solid angle, apart from some "dead" region, where CLAS can't measure due to presence of toroidal magnet, beamline etc. It consists of six identical sectors as shown in Figure **??**.

Each sector is a completely independent section and consists of Start

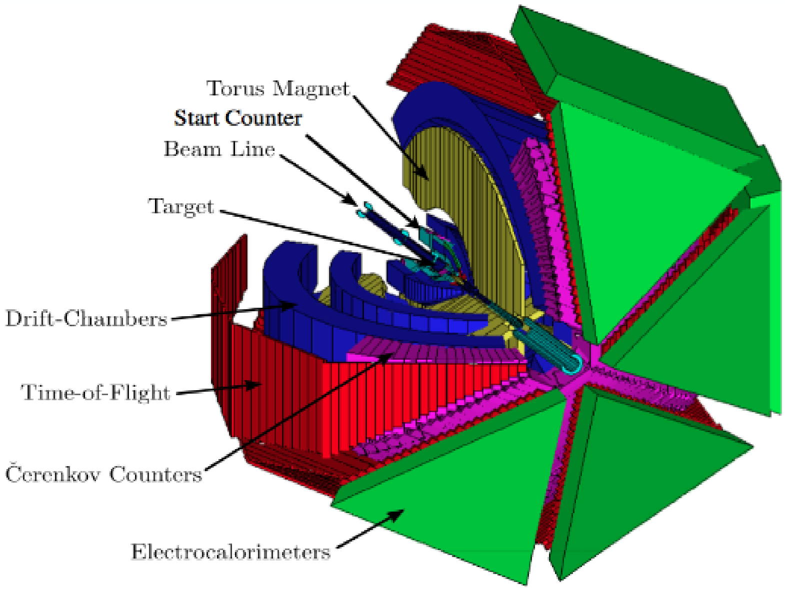

Figure 2.8: CLAS detector consists of six identical sectors

counter, Magnet for bending charged particles, Drift Chamber (DC), Time Of Flight (TOF) detector, Cerenkov Counter (CC), and Electromagnetic Calorimeter (EC).

2.3.1 Start Counter

Start counter is array of six identical sectors as shown in Figure **??**. Each sector consists of four scintillator paddle. It surrounds the target azimuthally. It measures the interaction time of incident photons in the target by detection of outgoing particles.

2.3.2 Toroidal Magnet (TM)

The toroidal magnet is of the main part of CLAS detector. Its six superconducting coils are arranged around the beamline, so that each have 60° separation in azimuthal direction. Moreover, because of kidney shape, the coil induces stronger magnetic field at forward angle of detector, hence the charged particles separate largely. The magnetic field associated with each sector is in the azimuthal direction and is always transverse to the parti-

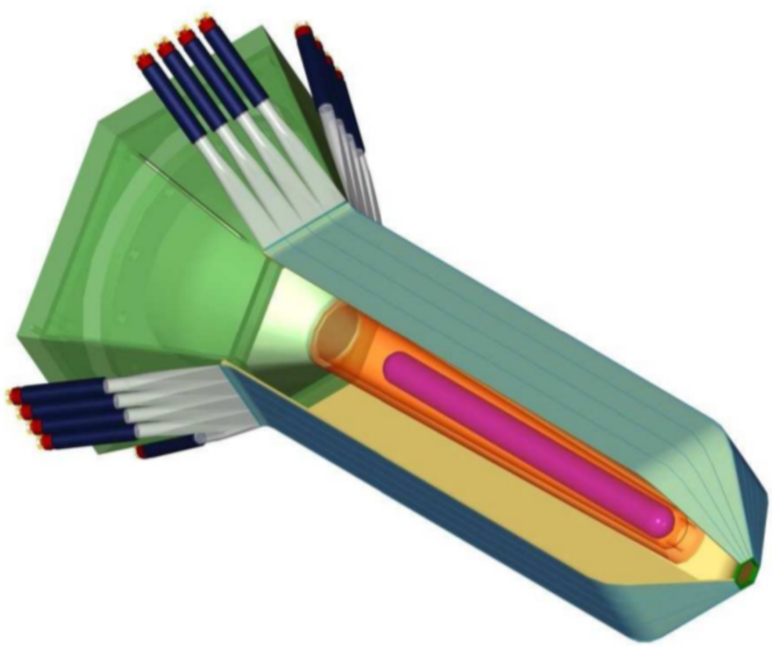

Figure 2.9: SC consists of six identical sectors, each sector consist four paddle.

cle's momentum. The field bends the trajectories of charged particles. So by knowing the strength of field one can obtain the momentum of particle. Figure **??** shows the shape of torous magnet that installed inside the CLAS. The relativistic cyclotron formula for particle momentum is

$$p = \frac{qBR}{c} \tag{2.3}$$

2.3.3 Drift Chamber (DC)

The drift chamber are used to measure trajectories of charged particles to measure their momenta. Similar to toroid DC consists of six identical sectors. Each sector itself consists three region as shown in Figure **??**. Every region consists of axial layers of wires. The axial layer measures scattering angle and momenta of particles. The DC system is filled with mixture of Ar and CO_2 gasses. The charged particles passing through it ionize the gas molecules. On applying opposite voltage one can find the information about drift time because of receiving ionized gasses through voltage.

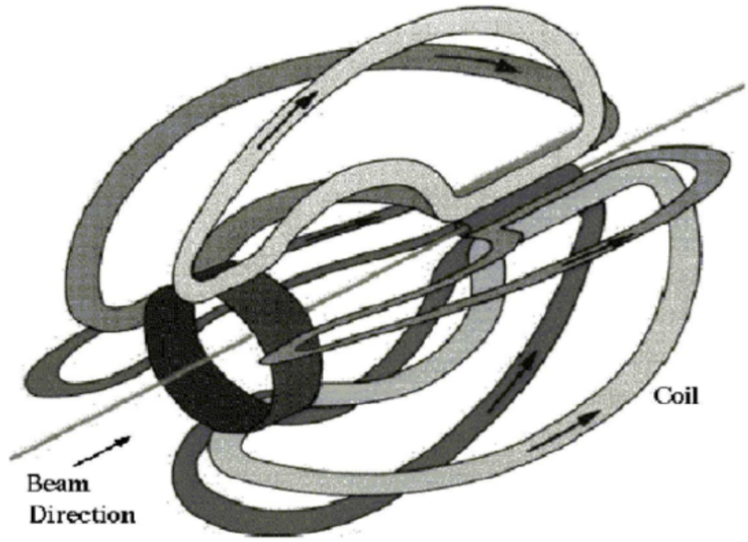

Figure 2.10: Superconducting toroid in six identical sectors to measure the momentum of charged particles.

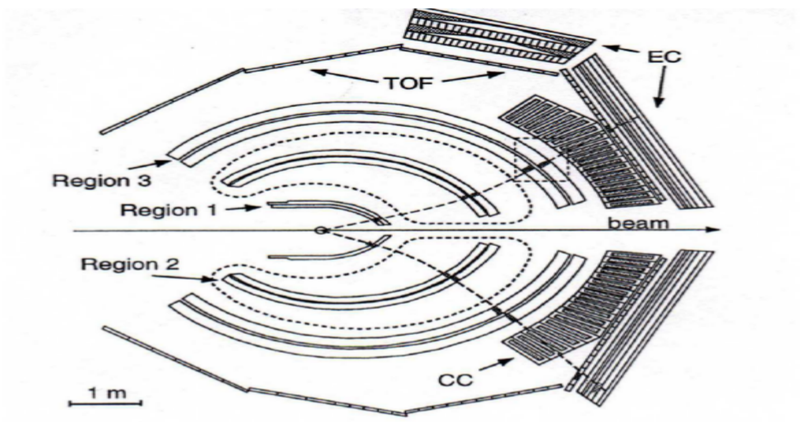

Figure 2.11: Drift Chamber filled with mixture of Ar and CO_2 gasses. Three region of DC are in different strength of magnetic field.

2.3.4 Time Of Flight (TOF)

Time Of flight detector is used to measure the time of flight of charged particles. The detector consist of 57 plastic scintillator of variable length as shown in Figure ??. When particles passes through it, they left track. By finding incoming time and outgoing time, we can determine the particle's velocity. So, it is possible to determine mass of the particle using the formula given below:

$$m = \frac{p\sqrt{1-\beta^2}}{\beta} \tag{2.4}$$

There are two additional detectors have been used in g12 experiment,

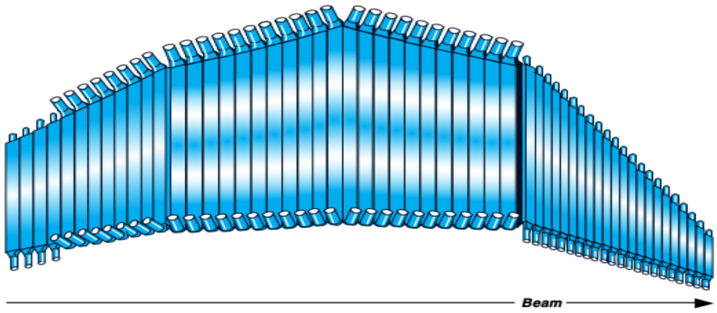

Figure 2.12: TOF detector used in CLAS to determine mass of particles.

Cerenkov Counter and Electromagnetic Calorimeter.

2.3.5 Čerenkov Counters (CC)

Working of Cerenkov Counter is based on Cerenkov radiation. Cerenkov radiation arises when the particle moves in the material medium with very high energy such a way that particle's speed is faster than the speed of light in the medium [?]. In such cases an electromagnetic shock wave is formed as shown Figure **??**. When charged particle moves with velocity v, in a dispersive medium of refractive index n, excited atoms in the vicinity of the particle get polarized. If v is greater than the speed of light in the medium c/n, a part of excitation energy reappears as coherent radiation emitted at characteristic angle θ to the direction of motion. The necessary condition is $v > c/n$ i.e. $n\beta > 1$ where $\beta = v/c$. By considering the produced wave form Figure **??** which gives (eq. **??**).

$$Cos\theta_c = \frac{1}{\beta n(\omega)} \tag{2.5}$$

So, depending upon their velocities the particles will left different shock wave by angle θ. That is, on the reverse way a determination of θ is direct measurement of the velocity. The Cerenkov counter is used to distinguish between lepton and pion. It is basically design to focus on cerenkov light coming from these particles, such that it polar angular coverage is ranging from 5° to 45°.

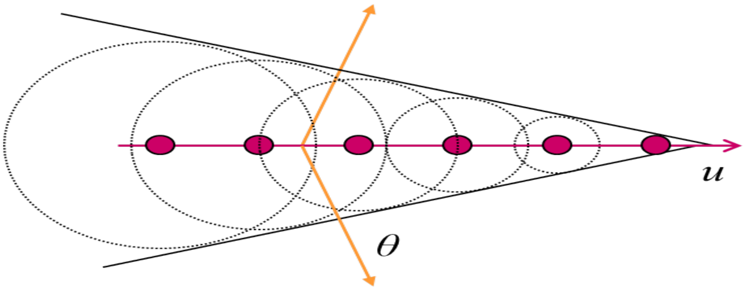

Figure 2.13: Shock wave of secondary wave with outgoing angle θ.

2.3.6 Electromagnetic Calorimeter (EC)

EC is very important class of detector for measuring position and energy of particles by technique of total absorption. Their role are more important when of particles energy are high. They differs from other detectors in that the nature of the particle is changed by detector , and as a fact of the matter they can detect neutral particles. What happens that during the absorption process, the particle will interact with material of the absorber, generating secondary particles; which will themselves generate further particles and so on, so that a shower or cascade Figure **??** develops. Due to production of secondary particles, eventually all the primary

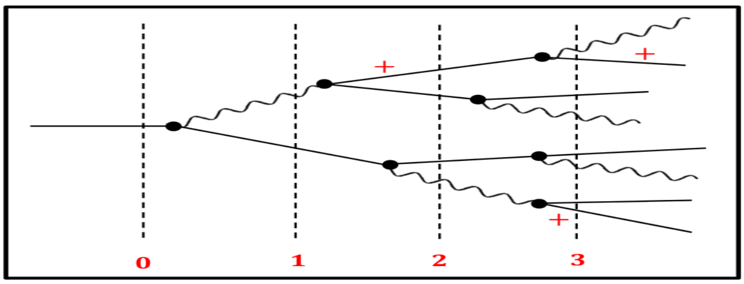

Figure 2.14: A cascade of secondary particles develops. All the energy is deposited on the material.

energy is deposited to medium, and finally it gives electrical signal using photomultiplier technique.

Chapter 3

Analysis

In this chapter we will discuss the definition of differential cross-section and the term associated with that, like missing mass and invariant mass etc. One of the main task in data analysis is to reduce background. So, we will discuss different conditions which have been implemented to get the clean signal from the decay channel $\eta^{'} \longrightarrow \pi^{+}\pi^{-}\eta$. No detector is hundred percent efficient, so one has to take the help of simulation to understand the detector efficiency for the particular channel. So, next we will discuss about the efficiency of the signal channel and different associated background channels from the simulation. Finally, we will calculate differential cross-section for small energy range.

3.1 Differential Cross-section

The purpose of this analysis is to determine the differential cross-section of the $\eta^{'}$ meson through the following decay channel:

$$\gamma + p \longrightarrow p + \eta^{'} \longrightarrow p + \pi^{+}\pi^{-}\eta(\eta \longrightarrow \gamma\gamma) \tag{3.1}$$

Differential cross-section of the $\eta^{'}$ meson [?] from the photoproduction experiment is defined as follows:

$$\frac{\mathrm{d}\sigma}{\mathrm{d}\Omega} = \frac{N_x}{A_x}\frac{1}{N_\gamma \rho_t}\frac{1}{\Delta\Omega}\frac{1}{BR(\eta^{'} \longrightarrow \eta\pi^{+}\pi^{-})} \tag{3.2}$$

where:

N_x: number of reconstructed $\eta^{'}$ meson in an (E_γ, cosθ_{cm}) bin

A_x: acceptance in an (E_γ, cosθ_{cm}) bin for the channel $\eta^{'} \longrightarrow \eta\pi^{+}\pi^{-}$

N_γ: number of beam photon in E_γ bin

ρ_t: target area density

$\Delta\Omega$: solid-angle interval ($2\pi\Delta cos\theta_{cm}$)

BR : branching ratio of the channel $\eta^{'} \longrightarrow \eta\pi^+\pi^-$

Few terms (N_x, A_x and N_γ) will be estimated in the following sections to get the differential cross-section.

3.1.1 Invariant Mass (IM)

Invariant mass is actually the intrinsic/proper mass of the particle or the system. On the other hand in case of bound state system it is simply the mass, is characteristic of total energy and momentum of the system. It is same for all frame of references, i.e. "Lorentz Invariant".

If one wants to calculate invariant mass of the $\eta^{'}$ meson from the decay channel $\eta^{'} \longrightarrow \eta\pi^+\pi^-$, experimentally one has to get energy momentum four vector of all final state particles (η, π^+, π^-). So, invariant mass of the $\eta^{'}$ meson ($IM_{\eta^{'}}$) is defined:

$$IM_{\eta'} = \sqrt{(p_{\pi^+} + p_{\pi^-} + p_\eta)^2} \tag{3.3}$$

Where p_{π^+}, p_{π^-} and p_η are the four momenta of π^+, π^- and η respectively. If we consider in centre of mass frame, the invariant mass is just total energy divided by square of the speed of light. In natural unit, since square root of four momentum square is the energy in CM frame.

3.1.2 Missing Mass (MM)

If experimentally we are unable to detect all the final state particles, in that scenario one can use missing mass technique to get the mass spectrum of the particles. Suppose in a particular reaction ($A + B \longrightarrow C + D$) if we know four momenta of A, B, C but the information of D is not fully known, one can determine the mass spectrum of the particle D by using energy momentum conservation.

$$A + B \longrightarrow C + D \tag{3.4}$$

$$p_A + p_B = p_C + p_D \Longrightarrow p_D = (p_A + p_B) - p_C \tag{3.5}$$

In persent analysis we have used four momentum of incoming photon, four momentum of target proton and four momentum of recoiled proton to determine the mass spectrum of the $\eta^{'}$ meson.

$$MM_{\eta'} = \sqrt{2m_p^2 + 2E_\gamma(m_p + P_p) - 2(E_\gamma + m_p)\sqrt{P_p^2 + m_p^2}} \tag{3.6}$$

where m_p is mass of proton, E_γ is beam energy and P_p is three momentum of recoil proton. Similarly, missing mass spectrum of η has been determined in the final state by using energy momentum.

3.1.3 Momentum Correction

The correction to the momentum of a particle introduced, due to unknown deviations in the magnetic field map that was used, during reconstruction of the particle's track [**?**], inside CLAS. The small deviations of the real field from the provided mapped field to the reconstruction software arises due to our limited knowledge of imperfections of the real field in CLAS as well as misalignment of drift chambers. This introduces small error in the calculated momentum of charged particles. Higher the multiplicity for the charged track in an event, higher the error in missing mass calculated for those events.

3.2 Overview of Technique Used

To determine the actual value of differential cross-section, we have used the following techniques.
(1) Calculate the production threshold energies of light mesons.
(2) Determine the missing mass off recoiled proton for reaction.

$\gamma + p \longrightarrow p + x$

(3) Study of outgoing proton and etaprime $\eta^{'}$ in Centre of Mass frame.

(4) Identify the peak of $\eta^{'}$ and η.

(5) Missing mass reconstruction of $\eta^{'}$ by applying condition on η and invariant mass of pions.

(6) Determine the $\eta^{'}$ meson yield in $cos(\theta)_{cm}^{\eta^{'}}$ with different CM energy using corrections.

3.2.1 Calculation of Production Threshold Energy

Production threshold energy of the $\eta^{'}$ meson along with other light mesons from the photoproduction reaction eq. (**??**) has been calculated

$$E_{\gamma} = \frac{m_x^2 + 2m_x m_p}{2m_p} \tag{3.7}$$

where m_p is mass of the proton, m_x is mass of the meson. So, threshold energy of the particle increases as the mass of corresponding particle increases.

S.N.	Particle	Mass(GeV/c^2)	Threshold Energy(GeV)
1	η	0.547	0.706
2	ω	0.782	1.10
3	$\eta^{'}$	0.957	1.445
4	ϕ	1.020	1.57

Table 3.1: Mass of mesons and their corresponding threshold energy in lab frame.

3.3 Data Analysis

The g12 data set was collected by the CLAS collaboration which is used for the current analysis. The raw data from different sub-detectors were then converted into the physical format from the digital hit information. This procedure is known as “cooking”. Moreover, the calibration was performed to optimize the particle track. The analysis begins with reconstructed events, the essential part of which are identification of particles and their corresponding momenta and energy. Using four momenta of incoming beam photon, target proton and recoiled proton, the missing mass spectrum of light mesons are plotted as shown in Figure ??. From the plot we can see, there are two major peaks and two small peaks with fairly smooth background. The first peak is in between 0.5-0.6 GeV/c^2, which is the peak of the η meson, second peak is for ω meson near 0.8 GeV/c^2, third peak is of η' meson near 0.95 GeV/c^2 and forth one is for ϕ meson near 1 GeV/c^2.

For the rough estimation of total number of the η' meson, we have selected

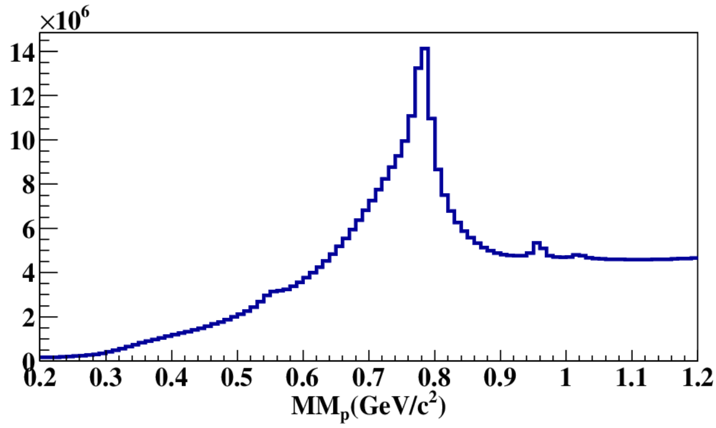

Figure 3.1: Missing Mass spectrum of mesons produced for energy range 1 GeV 5.5 GeV.

the missing mass range of the η' meson from 0.93-0.99 GeV/c^2 as shown in Figure ??. The histogram shows that still there is background in the peak region. To reduce the background, we have fitted the distribution with Gaussian (eq. ??) and second order polynomial (eq. ??).

$$G(X) = Ae^{-(X-\mu)^2/2\sigma^2} \tag{3.8}$$

where: A $= \frac{1}{\sigma\sqrt{2\pi}}$, μ is mean, σ sigma and a,b,c are parameters.

$$P(X) = aX^2 + bX + c \tag{3.9}$$

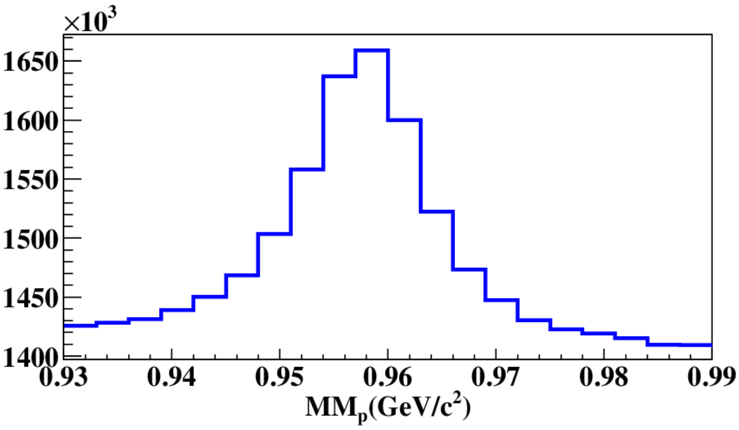

Figure 3.2: Missing Mass spectrum after selecting range around the $\eta^{'}$ meson.

The histogram shown in the Figure **??** is fitted histogram. The χ^2/ndf of the fitted distribution is 274/14 with mean and sigma 0.9577 GeV/c^2, 5.016 MeV/c^2 respectively, and the number of extracted $\eta^{'}$ mesons is 893571.

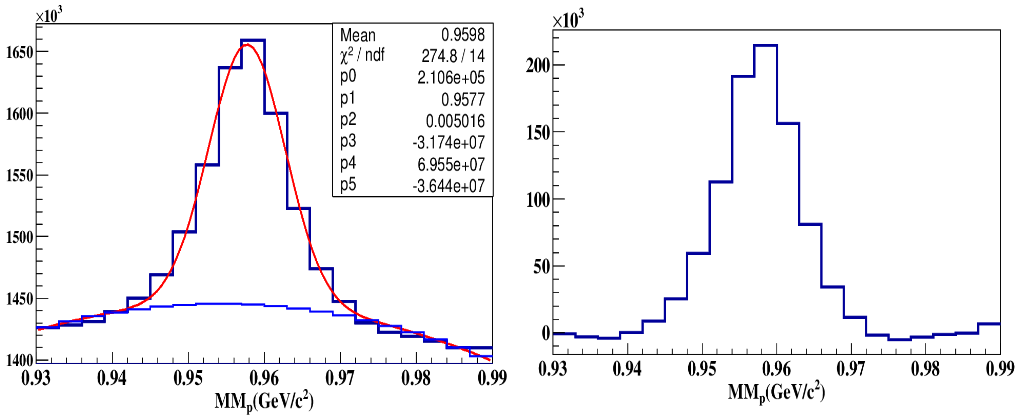

Figure 3.3: Missing mass of spectrum for range around the $\eta^{'}$ meson. The distribution is fitted with Gaussian and second order polynomial. The second one is yield of $\eta^{'}$ mesons after background subtraction.

3.3.1 Background Reduction

To determine the total number of $\eta^{'}$ mesons that undergo to the decay channel $\eta^{'} \longrightarrow \eta\pi^+\pi^-$, we put conditions on missing mass spectrum of the η meson and invariant mass of two charged pions to make sure that $\eta^{'}$ is coming from that decay channel. The distribution shown in Figure **??**

is missing mass spectrum of the η meson and invariant mass spectrum of pions. The mean and sigma after fitting the distribution with Gaussian and second order polynomial are 0.5487 GeV/c^2 and 0.010 GeV/c^2 respectively. In following analysis we will select missing mass spectrum of the η meson from 0.518-0.578 GeV/c^2. The histograms shown in Figure **??** are

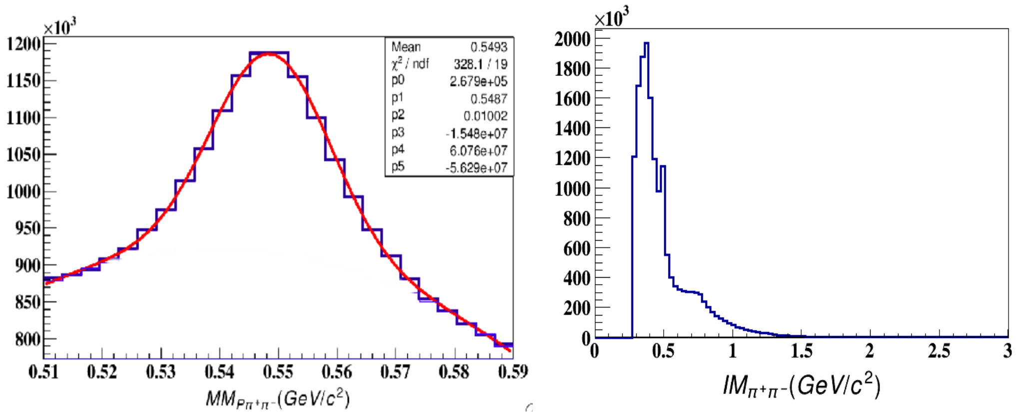

Figure 3.4: The first histogram is missing mass spectrum of the η meson, the second histogram is distribution of invariant mass of $\pi^+\pi^-$.

distributions of the η' meson after η mass cut. In the first histogram the distribution is only after the 3σ selection of the η. χ^2/ndf of the fitted distribution is 697.9/14 with mean and sigma 0.958 GeV/c^2, 5.2 MeV/c^2 respectively, and the number of extracted η' mesons is 252971. The second histogram of the Figure **??** is distribution of missing mass of η' after selecting 3σ range of η along with invariant mass of charged pions between (0.3-0.6 GeV/c^2). χ^2/ndf of the fitted distribution is 679.9/14 with mean and sigma 0.958 GeV/c^2, 5.2 MeV/c^2 respectively, and the number of extracted η' mesons is 247922.

In all above three cases although χ^2/ndf is very poor however our concern was the rough estimation of the number of η' mesons, so we did not concentrate that much of the χ^2/ndf value.

Table **??** shows a trend in the variation in the mean, sigma and number of η' mesons after applying different cuts. Here we can see large reduction in the number of η' mesons. These are some steps involve to rectify unwanted final state. We will take care of final step in further study, to proceed to

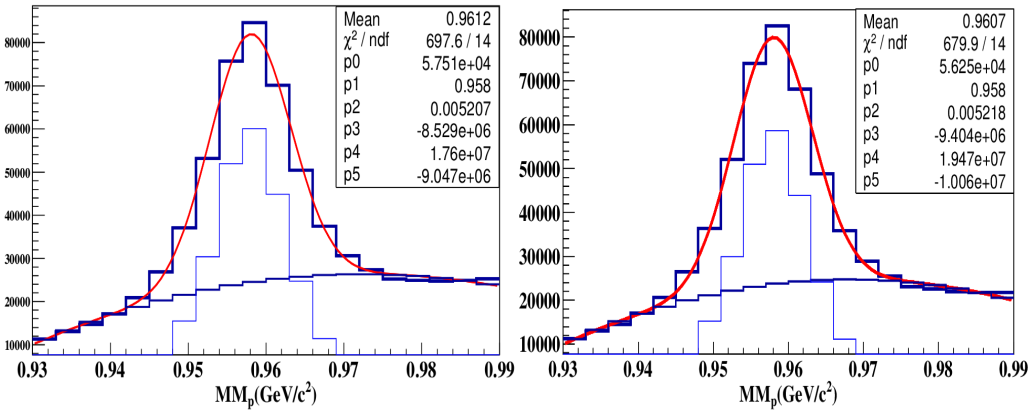

Figure 3.5: Missing mass spectrum of the $\eta^{'}$ meson after applying condition on 3σ range of the η meson and invariant mass of charged pions. The distribution is fitted with Gaussian and second order polynomial.

find differential cross-section.

S.N.	**Conditions Applied**	**Mean(μ)** GeV/c^2	**Sigma(σ)** MeV/c^2	**Extracted Yield**
1	No	0.957	5.016	893571
2	Missing($p\pi^+\pi^-$)	0.958	5.207	252971
3	Missing($p\pi^+\pi^-$), invariant($\pi^+\pi^-$)	0.958	5.218	247922

Table 3.2: Number of extracted $\eta^{'}$ mesons after applying different cuts.

3.3.2 Correction

Till now we have studied the data without momentum and track efficiency corrections. In the following section we will apply these corrections and we will monitor the variation of number of the $\eta^{'}$ mesons with these corrections one by one.

The histogram shown in Figure **??** is the distribution of missing proton. We have fitted the histogram with Gaussian and polynomial of order three. After applying momentum correction, χ^2/ndf of the fitted distribution is 965.6/13 with mean and sigma are 0.957 GeV/c^2, 5.0 MeV/c^2 respectively, and the number of extracted $\eta^{'}$ mesons is 632791.

After that we have applied track efficiency correction. Histogram shown in

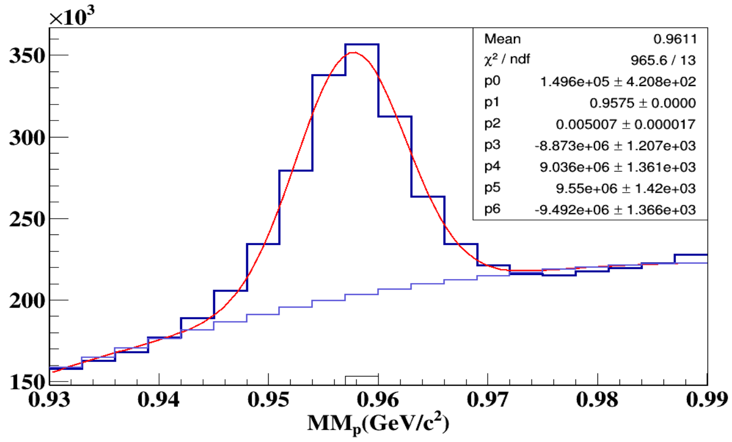

Figure 3.6: One dimensional histogram after momentum correction.

Figure **??** is missing proton spectrum after track efficiency correction. Histogram is fitted with Gaussian and third order polynomial. The χ^2/ndf of

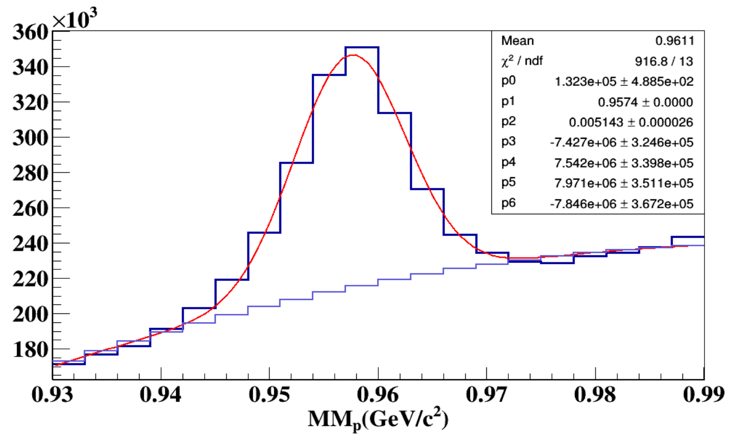

Figure 3.7: One dimensional histogram after applying track efficiency and momentum correction together.

the fitted distribution is 916.6/13 with mean and sigma are 0.957 GeV/c^2, 5.0 MeV/c^2 respectively, and the number of extracted $\eta^{'}$ mesons is 576539 . Here we can see there is huge reduction in the number of $\eta^{'}$ mesons after track efficiency correction as compare to the momentum correction.

Sometime the detector is unable to detect particles near the extrema of angle. To resolve that problem we have applied corrections, so that it will take care of angular inefficiency. Histogram shown in the Figure **??** is missing mass of proton after angular correction, together with track efficiency and momentum correction. Number of $\eta^{'}$ mesons within the 3σ

region is 240460.

Now we have completed all the corrections required for the data set. Table ?? shows the variation of number of the $\eta^{'}$ mesons after applying

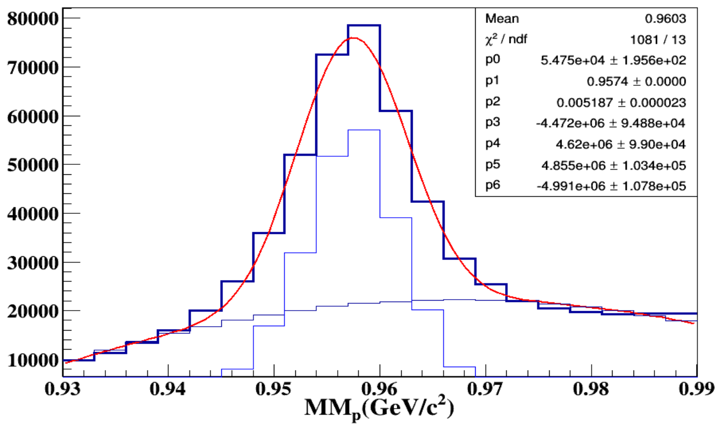

Figure 3.8: One dimensional histogram after applying angular correction, track efficiency, momentum correction.

the corrections one by one.

S.N.	Correction	Extracted Yield
1	Momentum	632791
2	Track efficiency	576539
3	Angular	240460

Table 3.3: Number of extracted $\eta^{'}$ mesons after applying different corrections.

3.3.3 Determination of the $\eta^{'}$ meson Yield for Differential Cross-section

In this section we will discuss variation of the number the $\eta^{'}$ mesons inside the peak region with $cos\theta_{cm}^{\eta^{'}}$ for particular beam energy range. To find that, we have plotted three dimensional histogram as shown in Figure ??. In this histogram we have filled missing mass of proton(MM_p) along the x-axis, $cos\theta_{cm}^{\eta^{'}}$ along the y-axis and centre of mass energy (W) along the z-axis. We have taken projection along the x-axis. The second histogram of Figure ?? is the projection along the missing mass axis. Histogram is fitted

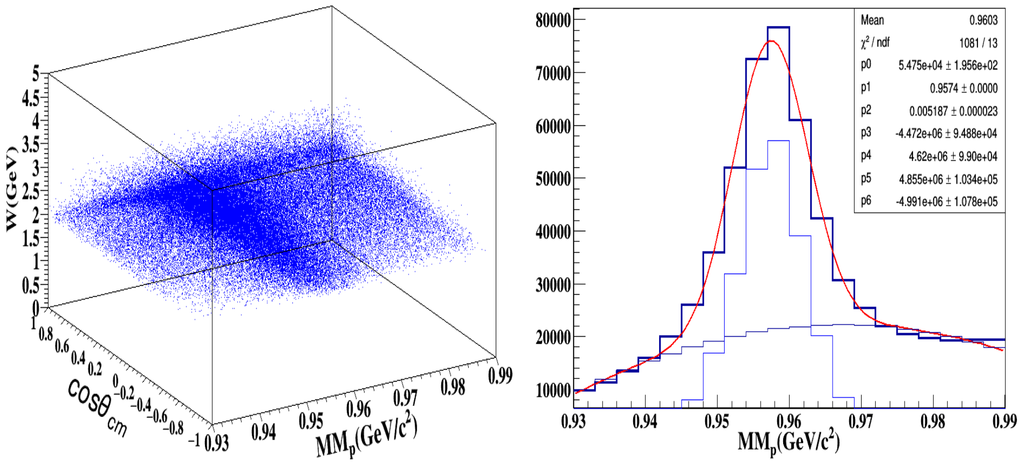

Figure 3.9: Three dimensional histogram after applying angular correction, track efficiency, momentum correction and all other conditions that were applied for background subtraction.

with Gaussian and polynomial of order three. Number of the η' mesons for W from 2.0 to 2.04 GeV is 240460 which is same as one dimensional way of determination of the η' mesons. The next job is to take the projections for $cos\theta_{cm}^{\eta'}$ from -1 to 1 at step of 0.1. The projection on the missing mass axis of histogram of Figure **??** for different $cos\theta_{cm}^{\eta'}$ is shown in Figure **??**. The variation of number of η' mesons with $cos\theta_{cm}^{\eta'}$ is shown in the Figure **??** and given in Table **??**.

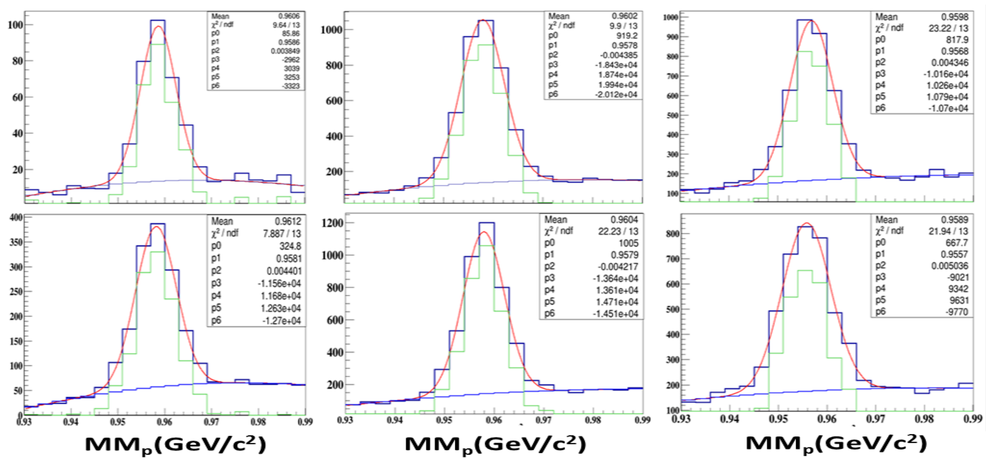

Figure 3.10: Projections of three dimensional histogram for different $cos\theta_{cm}^{\eta'}$ with beam energy W (2.0-2.04 GeV).

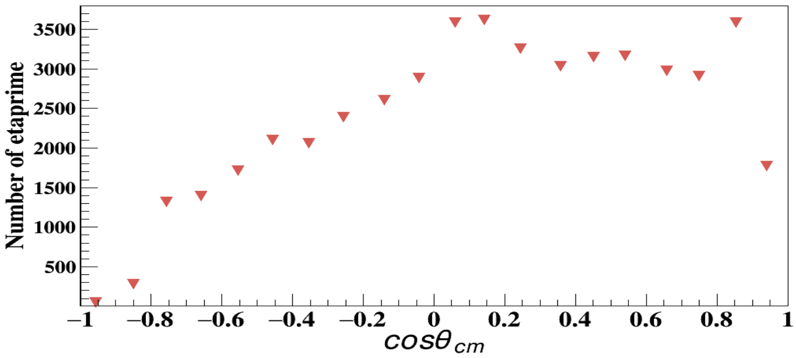

Figure 3.11: Variation of $\eta^{'}$ yield with $cos\theta_{cm}^{\eta^{'}}$ at step of 0.1.

S.N.	$\cos\theta_{cm}^{\eta^{'}}$	Extracted Yield
1	-0.95	17
2	-0.85	277
3	-0.75	1321
4	-0.65	1400
5	-0.55	1706
6	-0.45	2100
7	-0.35	2051
8	-0.25	2360
9	-0.15	2595
10	-0.05	2860
11	0.05	3600
12	0.15	3642
13	0.25	3266
14	0.35	3041
15	0.45	3127
16	0.55	3174
17	0.65	2995
18	0.75	2924
19	0.85	3605
20	0.95	1786

Table 3.4: Number of extracted $\eta^{'}$ mesons with $cos\theta_{cm}^{\eta^{'}}$ from -1 to 1 with a step of 0.1.

3.4 Simulation

Any detector is not hundred percent efficient. Therefore, to find the efficiency of detector one has to use the simulation technique. Also, to know the contributions of different background channels we need to do simulation. In the following section first we will discuss acceptance of the CLAS detector for the channel $\eta^{'} \longrightarrow \eta\pi^{+}\pi^{-}$. Secondly, we will find contribution due to in-peak background for the channel.

3.4.1 Acceptance

The CLAS detector in J-Lab installed in such a way that it can cover near 4π solid angle, though due to detector frame and beam holes, the practical acceptance is about 3π. The matter here is, the experiment is fixed target experiment, therefore beam photons in forward direction plays a defining role in acceptance of events that occur in collisions. Moreover due to construction of CLAS, it is unable to accept events in certain kinematical region. Asymmetry in acceptance is due to inefficient components, dead wires and small misalignment. Simulation also takes care of detector efficiency. Simulation reflects all these factors, which are due to CLAS detector setup, due to channel and due to any other physics involved.

There are some standard software tools for performing the simulation. In particular, analysis, a set of phase space weighted events, that are generally isotropically distributed, is generated. This process generates a set of four vector for event using phase weighted Monte Carlo, that satisfy the kinematical constrains like, the resonance mass, input beam energy and other. If physics specified during this process was all physics expected to observe, then these set of four-vectors would be kinematically distributed just like the real data. To simulate the detector effect, the generated four vectors are propagated through the virtual CLAS detector using software package called 'gsim'. Gsim takes information of each particle and creates a track for it through detector, and accordingly it has been detected similar to that of real data. That generated and reconstructed data are further used to determine the acceptance of the detector for the channel $\eta^{'} \longrightarrow \eta\pi^{+}\pi^{-}$. The following steps are taken to calculate acceptance for the channel eq.(**??**). In Figure **??** the first histogram is three dimensional histogram of generated data, whereas the second one is three dimensional histogram of reconstructed data after passing through virtual CLAS detector. Now in the next step we are going to find bin by bin acceptance.

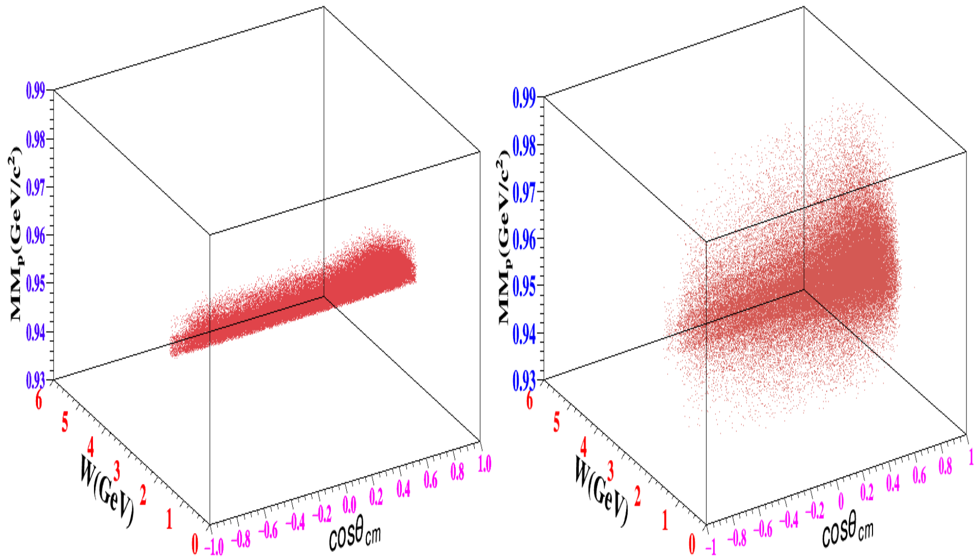

Figure 3.12: After applying angular correction, track efficiency, momentum correction and all other constrain. Three dimensional histogram for all energy and $cos\theta^{\eta'}_{cm}$ range for simulated data; where $cos\theta^{\eta'}_{cm}$ is on x-axis, W is on y-axis and missing proton is on z-axis.

Here basically we took projection of $cos\theta^{\eta'}_{cm}$ axis for generated and reconstructed events. Finally, we divided reconstructed histogram by generated histogram to find the acceptance. Figure **??** shows the acceptance of the detector for the channel $\eta' \longrightarrow \eta\pi^+\pi^-$. In this Figure **??**, we can see that, initially as $cos\theta^{\eta'}_{cm}$ increases from -1 to nearly 0, the value of acceptance increases from 2% to near 10%, further acceptance decreases up to 6% as the $cos\theta^{\eta'}_{cm}$ going towards 0.85.

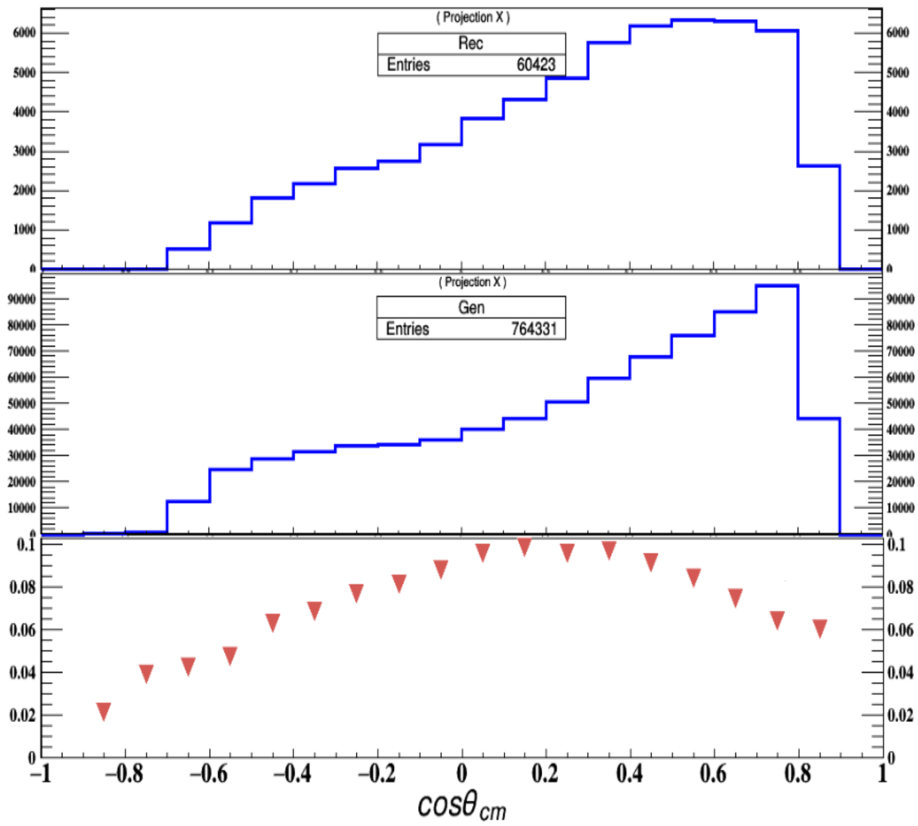

Figure 3.13: Variation of acceptance of the detector for the channel (eq. ??) with $cos\theta_{cm}^{\eta'}$ at a step of 0.1.

3.4.2 Background Study

We used simulation technique to find percentage contribution of in-peak background which is due to the channel $\eta' \longrightarrow \eta\pi^0\pi^0$. Here $\eta\pi^0\pi^0$ produces in-peak background if $\eta \longrightarrow \pi^+\pi^-\gamma$ and two pions produce 4γ. Then, in the final state we have $\pi^+\pi^-$ and 5γ. However, there are some undetected gammas. Therefore, it can give same final state as (eq. ??).

For finding the in-peak background we have followed similar way as we found the acceptance. As a rough estimation of in-peak background is nearly 10%.

3.5 Estimation of Differential Cross-section (DCS)

So far we have estimated total number of η' mesons for each $cos\theta_{cm}^{\eta'}$ bin shown in Figure **??**, and acceptance in Figure **??** for the same channel. Our next job is to find other terms associated with the differential cross-section (eq. **??**). Number of incoming photon, target density and height of target are tabulated in Table **??**. Using these parameters we found target area density ρ_t is 0.856/barn. We are now going to find differential cross-section

S.N.	N_γ (g/cm^3)	**Target Density** (g/cm^3)	**Height (cm)**	**BR**	$\Delta\Omega$
1	$8.013 * 10^{11}$	0.07114	40	43.3%	0.2π

Table 3.5: Parameters considered in our procedure.

for W from 2.0-2.04 GeV. The number of N_γ for this energy is $8.013 * 10^{11}$, so we can estimate $(1/\rho_t N_\gamma \Delta\Omega * BR)$ value for a particulr beam energy range W (2.0-2.04 GeV). To determine the variation of DC with $cos\theta_{cm}^{\eta'}$, we divided the histogram of number of η' vs $cos\theta_{cm}^{\eta'}$ by acceptance. Figure **??** shows the variation differential cross-section with $cos\theta_{cm}^{\eta'}$ for W from 2.0-2.04 GeV.

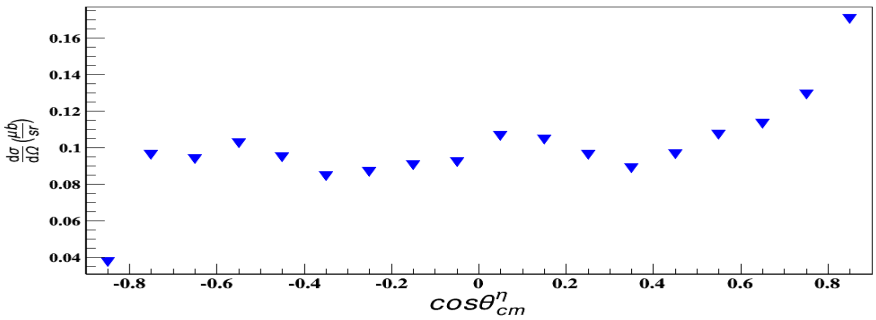

Figure 3.14: Variation of differential cross-section with $cos\theta_{cm}^{\eta'}$ at step of 0.1.

S.N.	$\mathbf{cos\theta^{\eta'}_{cm}}$	$DC(\mu b/sr)$
1	-0.85	0.037
2	-0.75	0.096
3	-0.65	0.094
4	-0.55	0.102
5	-0.45	0.094
6	-0.35	0.084
7	-0.25	0.086
8	-0.15	0.090
9	-0.05	0.092
10	0.05	0.106
11	0.15	0.104
12	0.25	0.095
13	0.35	0.089
14	0.45	0.096
15	0.55	0.106
16	0.65	0.113
17	0.75	0.129
18	0.85	0.170

Table 3.6: Variation of differential cross-section with $cos\theta^{\eta'}_{cm}$ at step of 0.1.

The variation of differential cross-section for different centre of mass energy is shown in Figure **??**. Here we can see for smaller values of W, the differential cross-section is approximately constant, but for higher values of W there is peak for larger values of $cos\theta^{\eta'}_{cm}$, on the other hand for some values of W there is peak in differential cross-section around smaller $cos\theta^{\eta'}_{cm}$. There are some theoretical aspect which could be behind these variations. We will discuss these in the next section.

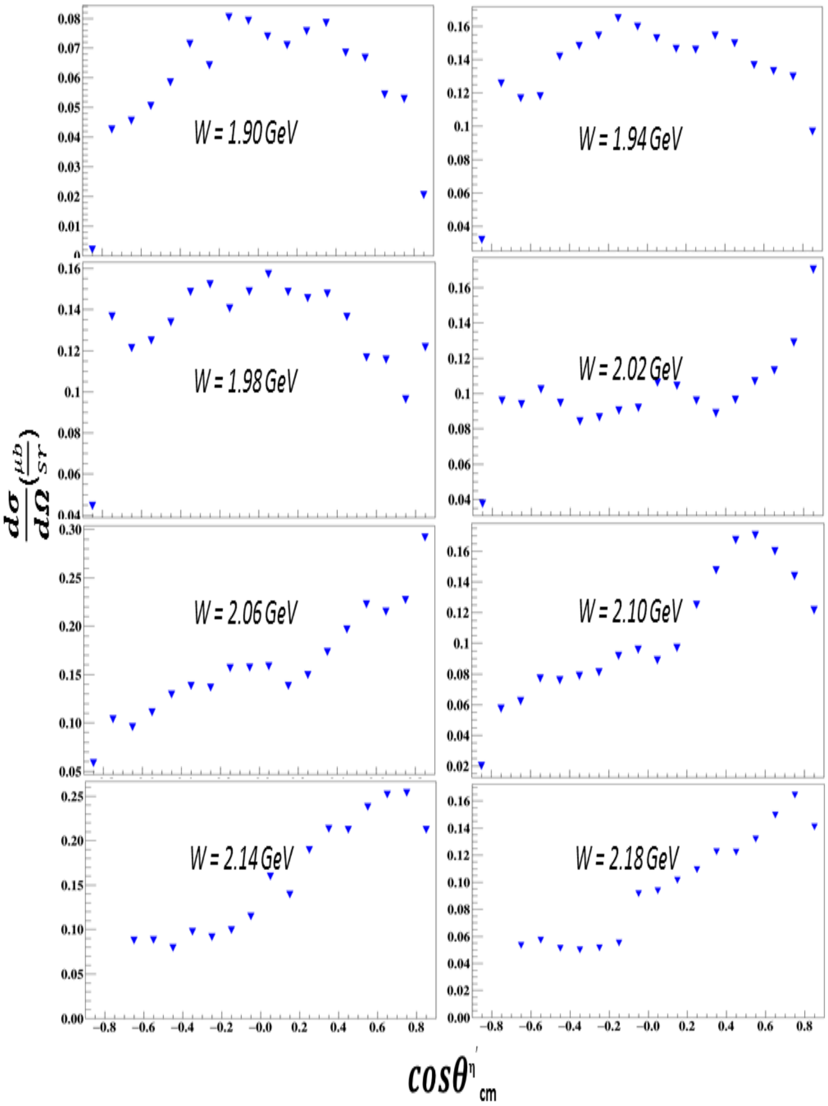

Figure 3.15: Variation of differential cross-section with $cos\theta_{cm}^{\eta'}$ at step of 0.1.

3.6 Error Analysis

In this section we will discuss errors associated with the analysis. There are two types of error involved, statistical error and systematic error. In this section, we will discuss the contribution of both errors for beam energy W from 2.0-2.010 GeV.

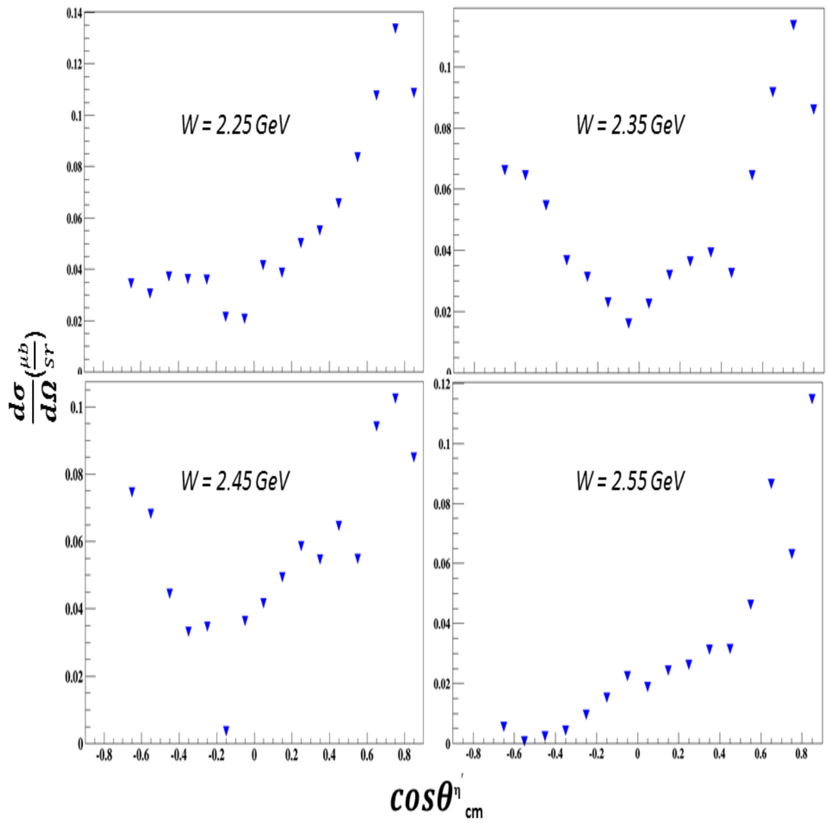

Figure 3.16: Variation of differential cross-section with $cos\theta^{\eta'}_{cm}$ at step of 0.1.

3.6.1 Statistical Error

The statistical error is the random error and depends on the statistics as the name suggests. The errors to the total number of the η' mesons in each $cos\theta^{\eta'}_{cm}$ bin, is inversely proportional to $\sqrt{N}$, where N is the number of η' mesons. However, due to vary large statistics the contribution of statistical error is very small as compare to systematic error. Therefore, in our analysis the systematical error dominates.

3.6.2 Systematic Error

The systematic error is basically the error due to system, means due to procedure of measurement of parameters and contribution due to implementation of different conditions. The main contribution of systematic errors can be due to:

(a) Selection of mass region in 3σ and in 2σ.

(b) Systematic effects in fitting.

(c) Systematic effects due to bin size.

The differential cross-section we have determined taking into account the total number of $\eta^{'}$ mesons in 3σ region of η and $\eta^{'}$ mesons. To find the systematic error we have determined differential cross-section changing σ region. Ideally, for both cases DCS should be same, if there is some uncertainty that will be accounted as systematic error. The analysis of other errors are still on the way. For finding DCS with W(2.0-2.010) we considered statistical and systematic due to contribution of mass selection.

After taking care of error contribution, the histogram shown in the Figure **??** is differential cross-section for W 2.0- 2.010 GeV.

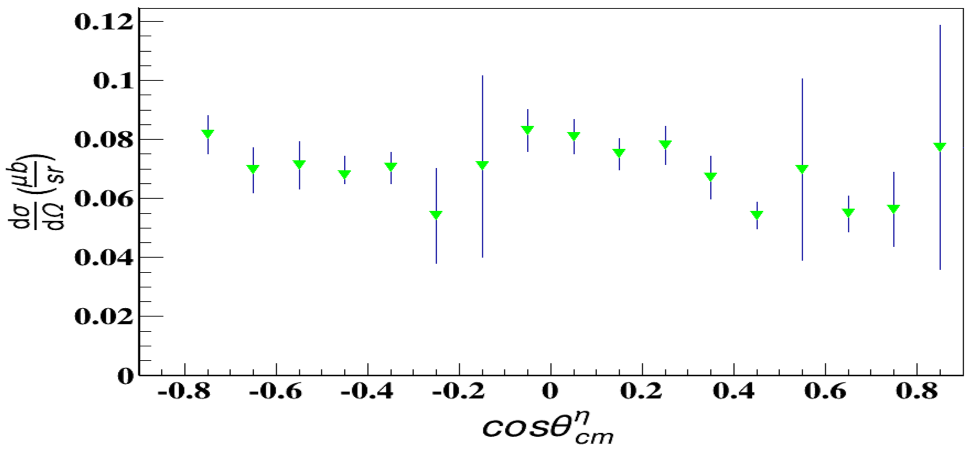

Figure 3.17: Variation of differential cross section with $cos\theta^{\eta'}_{cm}$ at step of 0.1.

3.7 Comparison of Differential Cross-section (DCS) with published result

In this section we have compared DCS with the published data [?]. There is published differential cross-section for g11 data [?]. In Figure **??** we have compared the differential cross-section with published data for beam energy W from 2.0-2.010 GeV and we took the ratio of published with our work. Ideally, the ratio should be one through out all $cos\theta^{\eta'}_{cm}$ range. We can see from upper plot in Figure ?? that for higher $cos\theta^{\eta'}_{cm}$ the DCS is lying within the error bars. However, there are some mismatch in lower values of $cos\theta^{\eta'}_{cm}$. It may be due to the in-peak background, poor acceptance in lower $cos\theta^{\eta'}_{cm}$ region and the data set was used till this analysis was 20% of whole data set. We will take into account all the above mentioned. Lower plot in Figure ?? is ratio of published DCS and reproduced DCS. Ratio infers that these are approximately comparable. Here we can also see that DCS is constant for all $cos\theta^{\eta'}_{cm}$.

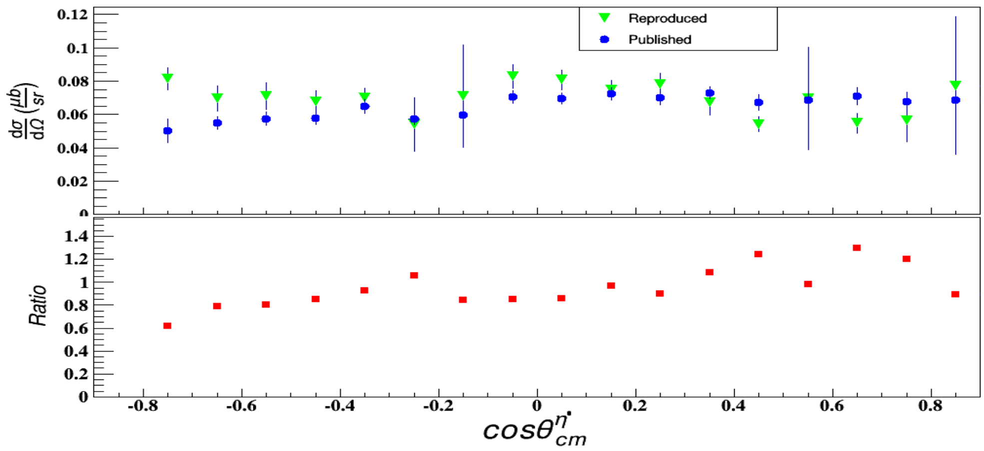

Figure 3.18: Variation of differential cross-section with $cos\theta^{\eta'}_{cm}$ at step of 0.1 for beam energy (W) from 2.0-2.010 GeV. Upper plot is comparison between published and our work. Lower plot is the ratio of reproduced and published.

3.8 Theoretical Explanation of Differential Cross-section (DCS)

In this section we would like to explain the behaviour of differential cross-section by using the concept of *Mandelstam variables*. For particular reaction $A + B \longrightarrow C + D$ the *Mandelstam variables* are:

$$s \equiv (p_A + p_B)^2/c^2$$
$$t \equiv (p_A - p_C)^2/c^2$$

$$u \equiv (p_A - p_D)^2/c^2$$

Where p_A, p_B, p_C, p_D are four momenta of particles A, B, C and D respectively,

Therefore, at the naive level, differential cross-section for s-channel, t-channel and u-channel are [?]:

$$\frac{d\sigma}{d\Omega} \propto \frac{\mathbf{1}}{\mathbf{W^2}},$$
$$\frac{d\sigma}{d\Omega} \propto \frac{\mathbf{1}}{\mathbf{W^2(1-\cos\theta)}}$$
$$\frac{d\sigma}{d\Omega} \propto \frac{\mathbf{1}}{\mathbf{W^2(1+\cos\theta)}}$$

The differential cross-section for the s-channel is only depend on centre of mass energy where as for t-channel, differential cross-section has larger peak along forward direction and for the u-channel, differential cross-section has larger peak along backward direction. Figure **??** shows one by one the variation in differential cross-section for s-channel, t-channel and u-channel. As we can see in s-channel differential cross-section is constant. So, for our

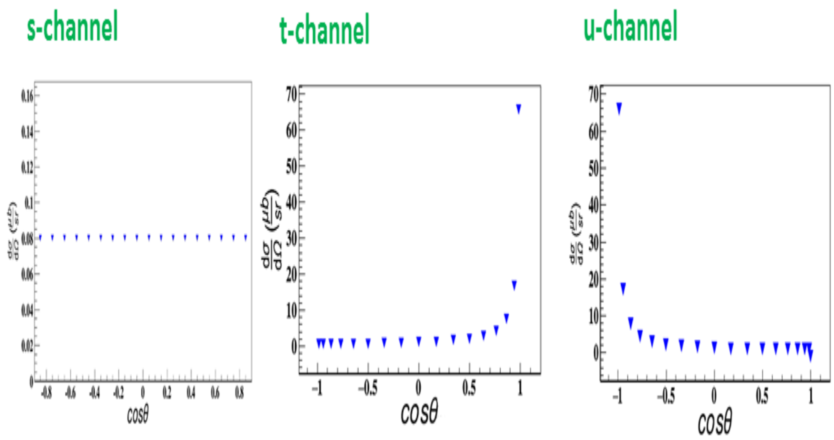

Figure 3.19: Variation of differential cross-section with $cos\theta$ for different channels.

case the constant variation at lower W, might be due to s-channel effect and in this scenario there could be only resonant state was involved in $\eta^{'}$ decay mode. On the other hand we can also infer that at larger slopes in forward and backward direction may be due to t-channel and u-channel effect respectively. So far we have analysed differential cross-section with

$cos\theta_{cm}^{\eta'}$ for different W. As we can see in Figure ?? for small values of W, differential cross-section is roughly constant, the fact of the matter might be due to only one resonance state contribution, and could be the contribution of s-channel. On the other hand for higher W, differential cross-section has forward and backward peak. The forward peak and backward peak may due to contribution of some other resonance states. These variations in differential cross-section infer that the effects might be due to t-channel and due to u-channel.

3.9 Summary and Future Outlook

In this section we will briefly discuss the results we have obtained so far and we will discuss about our future work.

3.9.1 Summary

We have discussed the variation of the number of $\eta^{'}$ mesons and we have plotted histogram of number of $\eta^{'}$ vs $cos\theta_{cm}^{\eta'}$ as shown in Figure ??. We did simulation to estimate acceptance of the channel $\eta^{'} \longrightarrow \eta\pi^{+}\pi^{-}$. The acceptance was about $2 - 10\%$ with $cos\theta_{cm}^{\eta'}$. In the later section we have determined differential cross-section (DCS) with $cos\theta_{cm}^{\eta'}$ variation with different beam energies. We have explained the behaviour of differential cross-section for lower values of beam energy. For higher beam energy the peak at angular boundaries tantalizing the fact that there might be contributions due to some other channel or interference due to other resonance modes. Finally, we have compared with previous publication.

3.9.2 Future Outlook

This analysis was performed with 20% of whole g12 data. So, in future we will determined differential cross-section for whole g12 data. We will study all systematic errors and reduces the contribution of in-peak background due to channel $\eta^{'} \longrightarrow \eta\pi^{0}\pi^{0}$. We will reproduce differential cross-section for same energy range and at the end of the day we will find differential cross-section for the higher beam energy regime.

Bibliography

[1] David Griffiths, Introduction to Elementary Particles.

[2] A.Klein Phys.Rev 99,998(1995).

[3] H.Seraydaryan Phys. Rev.C 89,055206(2014)

[4] G.Sterman *et al.*, Rev. Mod. Phys.67,157(1995)

[5] G.R.Farrar *et al.*, Nucl. Phys. B 349,665(1991)

[6] A.H. Mueller, Phys. Rep. 73,237(1981)

[7] https://www.jlab.org/accelerator-science

[8] Michael Dugger Thesis on Eta and Etaprime photoproduction.

[9] Brian Martin Nuclear and Particle Physics.

[10] V.Crede *et al.*(TAPS) Phys. ReV. C(80, 045213)(2009)

[11] Particle Data Group

[12] J.Goetz CLAS g12 analysis note, November(2012)

[13] M.Williams *et al.*(CLAS)Phys.Rev.C(80,045213)(2009)

[14] Michoel E. Peskin, An Introduction To Quantum Field Theory